



Fluorine in the Solar Neighborhood: The Need for Several Cosmic Sources

Nils Ryde¹ , Henrik Jönsson^{1,2} , Gregory Mace³ , Katia Cunha^{4,5} , Emanuele Spitoni⁶ , Melike Afşar⁷ , Daniel Jaffe³ ,
Rebecca Forsberg¹ , Kyle F. Kaplan⁸ , Benjamin T. Kidder³ , Jae-Joon Lee⁹ , Heeyoung Oh^{9,10} , Verne V. Smith¹¹ ,
Christopher Sneden³ , Kimberly R. Sokal³ , Emily Strickland³, and Brian Thorsbro¹ 

¹Lund Observatory, Department of Astronomy and Theoretical Physics, Lund University, Box 43, SE-221 00 Lund, Sweden; ryde@astro.lu.se

²Materials Science and Applied Mathematics, Malmö University, SE-205 06 Malmö, Sweden

³Department of Astronomy and McDonald Observatory, The University of Texas, Austin, TX 78712, USA

⁴Observatório Nacional San Cristóvão, Rio de Janeiro, Brazil

⁵University of Arizona, Tucson, AZ 85719, USA

⁶Stellar Astrophysics Centre, Department of Physics and Astronomy, Aarhus University, Ny Munkegade 120, DK-8000 Aarhus C, Denmark

⁷Department of Astronomy and Space Sciences, Ege University, 35100 Bornova, İzmir, Turkey

⁸SOFIA Science Center, Universities Space Research Association, NASA Ames Research Center, MS 232-12, Moffett Field, CA 94035, USA

⁹Korea Astronomy and Space Science Institute, 776, Daedeok-daero, Yuseong-gu, Daejeon, 34055, Republic of Korea

¹⁰Department of Astronomy, University of Texas at Austin, Austin, TX 78712, USA

¹¹National Optical Astronomy Observatories, Tucson, AZ 85719, USA

Received 2019 December 19; revised 2020 February 26; accepted 2020 March 9; published 2020 April 14

Abstract

The cosmic origin of fluorine is still not well constrained. Several nucleosynthetic channels at different phases of stellar evolution have been suggested, but these must be constrained by observations. For this, the fluorine abundance trend with metallicity spanning a wide range is required. Our aim is to determine stellar abundances of fluorine for $-1.1 < [\text{Fe}/\text{H}] < +0.4$. We determine the abundances from HF lines in infrared *K*-band spectra ($\sim 2.3 \mu\text{m}$) of cool giants, observed with the IGRINS and Phoenix high-resolution spectrographs. We derive accurate stellar parameters for all our observed *K* giants, which is important as the HF lines are very temperature-sensitive. We find that $[\text{F}/\text{Fe}]$ is flat as a function of metallicity at $[\text{F}/\text{Fe}] \sim 0$, but increases as the metallicity increases. The fluorine slope shows a clear secondary behavior in this metallicity range. We also find that the $[\text{F}/\text{Ce}]$ ratio is relatively flat for $-0.6 < [\text{Fe}/\text{H}] < 0$, and that for two metal-poor ($[\text{Fe}/\text{H}] < -0.8$), *s*-process element-enhanced giants, we do not detect an elevated fluorine abundance. We interpret all of these observational constraints as indications that several major processes are at play for the cosmic budget of fluorine over time: from those in massive stars at low metallicities, through the asymptotic giant branch star contribution at $-0.6 < [\text{Fe}/\text{H}] < 0$, to processes with increasing yields with metallicity at supersolar metallicities. The origins of the latter, and whether or not Wolf–Rayet stars and/or novae could contribute at supersolar metallicities, is currently not known. To quantify these observational results, theoretical modeling is required. More observations in the metal-poor region are required to clarify the processes there.

Unified Astronomy Thesaurus concepts: [Infrared astronomy \(786\)](#); [High resolution spectroscopy \(2096\)](#); [Chemical abundances \(224\)](#); [Cosmic abundances \(315\)](#); [Stellar abundances \(1577\)](#)

1. Introduction

The cosmic origin of fluorine, i.e., the sites and processes that are responsible not only for the buildup of the element in the universe but also its galactic chemical evolution, is still very uncertain and turns out to be very intriguing. The solar abundance of fluorine is less than a percent of that of neighboring elements in the periodic table, which is a reflection of its unique formation channels. Fluorine reacts readily with hydrogen and helium in stellar interiors, via the reactions $^{19}\text{F}(p, \alpha)^{16}\text{O}$ and $^{19}\text{F}(\alpha, p)^{22}\text{Ne}$, which destroy the ^{19}F nuclei. There are, however, several possible nucleosynthetic reaction chains acting in different evolutionary processes of stars that can synthesize the fragile fluorine nuclei so that they survive and contribute to the buildup of the cosmic reservoir of fluorine. It is debated which of the possible processes is dominant in the universe and their relative importance at different epochs. Measuring fluorine abundances as a function of time or metallicity provides important constraints on the different formation channels and different theories of the formation of fluorine.

Several of the theoretically suggested processes (see, e.g., the discussion in Spitoni et al. 2018) could actually, within

their uncertainties and reasonable ranges of input parameters, by themselves produce all of the measured cosmic fluorine abundance. However, the different processes act on different timescales, which means that the evolution of the buildup of fluorine will be very different. Observational constraints on these evolutionary trends will test the importance of the processes. The observed trends might also reflect several processes and might be different for different stellar populations (for example, the thin-disk, thick-disk, and bulge populations). At low metallicities, the ν process (Woosley & Haxton 1988) and the contribution from rapidly rotating, massive stars (Prantzos et al. 2018) can be tested. At solar metallicities, the contribution from the thermally pulsating asymptotic giant branch (TP-AGB) stars (Jorissen et al. 1992) will be the largest, and at higher metallicities, and especially at supersolar metallicities, the contributions from novae (Spitoni et al. 2018), Wolf–Rayet stars (Meynet & Arnould 2000), or from some other metallicity-dependent process might become increasingly strong. Whether or not Wolf–Rayet stars actually would contribute to the cosmic budget of fluorine is, however, highly uncertain (Palacios et al. 2005 and G. Meynet 2020, private communication).

However, determining the fluorine abundance is challenging. There is only one stable isotope, ^{19}F , and no useful atomic lines are readily available for an abundance determination in cool, stellar atmospheres. The highly ionized lines in the far-UV (Werner et al. 2005) and the highly excited F I lines at 6800–7800 Å are only observed in hot stars. The latter were used in extreme helium stars and R Coronae Borealis stars (Pandey 2006; Pandey et al. 2008), with temperatures of $T_{\text{eff}} > 6500$ K. The only readily useful diagnostics are lines from the HF molecule in the K and N bands (2.1–2.4 μm and 8–13 μm , respectively), lines which are observable only in cool giants ($T_{\text{eff}} < 4500$ K). In the K band, telluric lines can render the abundance determinations uncertain (de Laverny & Recio-Blanco 2013). The molecular lines are also sensitive to the effective temperatures of the stars, which therefore have to be determined with high accuracy. The diagnostically interesting metal-poor region (investigating the role of and yields from rapidly rotating massive stars and/or the ν process) is very difficult to address observationally. The HF line lists, both for vibration–rotation lines in the K band, as well as the pure rotational lines in the N band, including the needed partition functions, are now well determined; see the discussions in Jönsson et al. (2014a, 2014b).

The field of observationally investigating the chemical evolution of fluorine has grown in recent years due to the advent of sensitive, high-resolution spectrometers recording light in the infrared; for example, Recio-Blanco et al. (2012) and Jönsson et al. (2014a) used CRIRES at the Very Large Telescope and Pilachowski & Pace (2015), Jönsson et al. (2017b), and Guerço et al. (2019a, 2019b) used the Phoenix spectrometer to measure fluorine abundances in K -band spectra. Guerço et al. (2019a) also used iSHELL at the NASA Infrared Telescope Facility (IRTF). Furthermore, Jönsson et al. (2014b) used TEXES spectra to measure abundances from the rotational lines at 12 μm as well as archival, K -band spectra observed with the Fourier Transform Spectrometer at Kitt Peak National Observatory. Theoretical work during the most recent years include those of Prantzos et al. (2018), Spitoni et al. (2018), and Olive & Vangioni (2019), apart from work done on the nucleosynthetic reaction rates (Sieverding et al. 2018, 2019; Langanke et al. 2019). A more detailed discussion of these recent investigations and their interpretation will be given in Section 5.2. The investigation of the cosmic budget of fluorine is very active and will still require more observational and theoretical work in the future.

Here, we analyze the fluorine abundances in 61 stars with carefully and homogeneously determined stellar parameters. The latter is important to minimize the systematic uncertainties inherent to the used HF line. In this way, we will be able to provide the largest set of homogeneously determined fluorine abundances for a range of metallicities. We analyze new K -band spectra observed with the Immersion GRating INfrared spectrograph (IGRINS; Yuk et al. 2010; Park et al. 2014) and reanalyze K -band spectra observed with the Phoenix spectrograph, using more accurate stellar parameters. The spectra from both instruments have very similar spectral resolving powers and signal-to-noise ratios. The purely rotational HF lines at 12 μm , presented in Jönsson et al. (2014b), are stronger than the vibration–rotation lines at 2.3 μm (K band), and should be explored further in the future for an abundance investigation of cool giants in the metal-poor region. Observations at 12 μm require, however, brighter stars, due to insufficiently sensitive

spectrographs and less light from stars in the N band (Jönsson et al. 2014b).

2. Observations and Data Reduction

Our goal is to fill in and expand the fluorine trends presented in Jönsson et al. (2017b) for $-0.5 < [\text{Fe}/\text{H}] < 0.4$, especially expanding the metallicity range both downward and upward. We have selected such stars from a careful optical analysis of about 500 giants to be presented in H. Jönsson et al. (2020, in preparation). These stars are all warmer than 4000 K (K giants), and we therefore avoid the AGB stars that can produce fluorine themselves and pollute their atmospheres (see, e.g., Jorissen et al. 1992). Hence, all our stars are useful probes for the galactic chemical evolution of fluorine.

Because the fluorine abundances are determined from vibration–rotational lines of the HF molecule, stars that yield suitable HF line strengths have to be chosen. For a given metallicity, these molecular lines become stronger the cooler the star is and the lower the surface gravity of the star is; the lower the temperature is, the larger is the molecular density, and the lower the surface gravity is, the stronger is the relative strength of the lines compared to the continuum. The continuum opacity in this wavelength region, which is due to the H_{ff} process, decreases with electron pressure in the line-forming regions, which in turn decreases with lower surface gravities. Because the line strengths are proportional to the ratio of line to continuum opacities, the lines become stronger for a star with a lower surface gravity, for a given fluorine abundance (see Jönsson et al. 2014a). Thus, in order for the lines to be measurable in stars of low metallicities, cool giants should be chosen. In the metal-rich wavelength region, the lines can even become saturated for very cool giants.

Spectra of giants from two sets of observations have been analyzed here: the first set consists of 25 giants, which were observed with the IGRINS spectrograph (Yuk et al. 2010). Of these giants, 10 had spectra with a detectable HF feature and another 10 yielded a useful upper limit. The second set consists of 41 giants with spectra from Jönsson et al. (2017b) displaying a detectable HF line and are reanalyzed here. These were observed with the Phoenix spectrograph (Hinkle et al. 1998, 2003) mounted on the 4 m Mayall telescope at Kitt Peak National Observatory (KPNO) at a spectral resolving power of $R = 50,000$ and typical signal-to-noise ratios of 100 (for more details, see Jönsson et al. 2017b).

We have also used the derived abundances from six giants from the work by Jönsson et al. (2014b). They observed these stars with the TEXES spectrograph (Lacy et al. 2002) at NASA’s Infrared Telescope Facility (IRTF), recording the rotational HF lines at 12 μm with a spectral resolving power of $R \sim 65,000$ and a signal-to-noise ratio also of typically 100. They used a similar method of analysis to that presented here.

The IGRINS spectra were recorded during 2016, from February to December, apart from α Boo, which was observed earlier on 2015 April 11; see Table 1. The spectra were all observed on the 4.3 m Discovery Channel Telescope (DCT) at Lowell Observatory (Mace et al. 2018), or on the 2.7 m Harlan J. Smith Telescope at McDonald Observatory (Mace et al. 2016). IGRINS provides a spectral resolving power of $R = \lambda/\Delta\lambda \sim 45,000$ spanning the full H and K bands (1.45–2.5 μm), recorded in one exposure, even though for this paper we use only small parts of the spectra.

Table 1
IGRINS Observing Log in the Same Order as in Table 2

Star	2MASS Name	H	K	Date	Telescope	Exposure Time
(1)	(2)	(mag)	(mag)	(5)	(6)	(s)
		(3)	(4)			(7)
Stars with a detected HF line:						
HIP 72012	J14434444+4027333	2.6	2.4	2016 Jun 16	HJST	30 × 4 (ABBA)
KIC 5113061	J19413439+4017482	8.2	8.0	2016 Nov 22	DCT	90 × 8 (ABBAABBA)
HIP 63432	J12595500+6635502	2.4	2.1	2016 May 29	HJST	30 × 6 (ABBAAB)
HIP 96014	J19311935+5018240	2.9	2.5	2016 Jun 15	HJST	30 × 4 (ABBA)
KIC 5779724	J19123427+4105257	8.0	7.8	2016 Dec 9	DCT	60 × 10 (ABBAABBAAB)
KIC 4177025	J19434309+3917436	7.6	7.5	2016 Nov 22	DCT	60 × 6 (ABBAAB)
KIC 5113910	J19421943+4016074	8.2	8.0	2016 Nov 22	DCT	90 × 8 (ABBAABBA)
KIC 3955590	J19272677+3900456	7.8	7.7	2016 Nov 23	DCT	60 × 8 (ABBAABBA)
HD 102328	J11465561+5537416	2.9	2.6	2016 Feb 2	HJST	1.6 × 20 (A & B)
KIC 5900096	J19515137+4106378	6.0	5.8	2016 Nov 22	DCT	30 × 4 (ABBA)
Stars yielding an upper limit of the HF abundance:						
HIP 50583	J10195836+1950290	−0.8	−0.8	2016 Jun 20	HJST	1.6 × 18 (A)
KIC 11045542	J19530590+4833180	8.4	8.2	2016 Dec 11	DCT	250 × 8 (ABBAABBA)
α Boo	J14153968+1910558	−2.8	−2.9	2015 Apr 11	HJST	30 × 2 (AB)
2M14231899	J14231899+0540079	8.0	7.8	2016 Jun 19	HJST	150 × 8 (ABBA)
2M17215666	J17215666+4301408	7.6	7.5	2016 Jul 25	HJST	180 × 6 (ABBAAB)
KIC 4659706	J19324055+3946338	7.6	7.4	2016 Nov 19	DCT	60 × 8 (ABBAABBA)
HIP 90344	J18255915+6533486	2.2	2.1	2016 Jun 15	HJST	30 × 4 (ABBA)
KIC 3936921	J19023934+3905592	8.3	8.1	2016 Nov 23	DCT	120 × 8 (ABBAABBA)
KIC 11342694	J19110062+4906529	7.6	7.4	2016 Nov 17	DCT	60 × 8 (ABBAABBA)
KIC 3748585	J19272877+3848096	6.4	6.3	2016 Nov 17	DCT	30 × 8 (ABBAABBA)

Note. DCT: the Discovery Channel Telescope, a 4.3 m telescope at Lowell Observatory, Arizona. HJST: the Harlan J Smith Telescope, a 2.7 m telescope at McDonald Observatory, Texas.

The stars were observed in an ABBA nod sequence along the slit. Exposure times for these bright objects range from 30 to 2000 s; see Table 1. These exposure times were set by the requirement to retrieve spectra of a signal-to-noise ratio of at least 100, which was achieved. Telluric standard stars (typically rapidly rotating, late-B to early-A dwarfs) were also observed in conjunction with the science targets at similar air masses. All the spectra were reduced using the IGRINS pipeline (Lee et al. 2017), which extracts wavelength-calibrated spectra after flat-field correction and A-B frame subtractions.

The science spectra were then divided by the telluric spectra, in order to divide out the telluric lines. This works very well, because the telluric stars are observed close in time and at a similar airmass compared to the observations of the science targets. Every order of the divided spectra is continuum normalized with the IRAF task `continuum` (Tody 1993). These were then combined with the task `scombine` allowing an addition of overlapping regions of subsequent orders, but also cutting away edge regions with no traceable continuum and spurious edge effects. This resulted in one normalized stitched spectrum for the K band with a wavelength coverage of 19700–24800 Å. The regions with heavy telluric contamination at the edges of these limits are, however, not always useful. In the cases where the final spectra still have some modulation in their continuum levels, these are taken care of by defining specific local continua around the spectral line being studied. The HF line that is finally used lies at $\lambda_{\text{air}} = 23358.33$ Å. The 10 spectra with a detected HF line are shown in Figure 1, where the spectra are ordered by increasing T_{eff} . The effective temperatures and metallicities of the stars are indicated in the figure.

3. Analysis

From the IGRINS spectra of these 10 new stars and the 41 Phoenix spectra, we have thus derived the fluorine abundance from the HF($v = 1 - 0$) R9 line at $\lambda_{\text{air}} = 23\,358.33$ Å. We have analyzed these spectra with tailored synthetic spectra, calculating the radiative transfer through spherical model atmospheres, defined by their stellar parameters. These are the effective temperature, T_{eff} , surface gravity, $\log g$, metallicity, $[\text{Fe}/\text{H}]$, and the microturbulence, ξ_{micro} .

In order to derive abundances as accurate as possible, these fundamental input parameters must be determined accurately and in a homogeneous way. The spectroscopic method developed for K giants from high-resolution optical spectra by Jönsson et al. (2017a) can do that. In this method, the stellar parameters are determined simultaneously by fitting unsaturated and unblended Fe I, Fe II, and Ca I lines as well as $\log g$ sensitive Ca I wings. The derived parameters are benchmarked against independently determined effective temperatures, T_{eff} , from angular diameter measurements and surface gravities, $\log g$, from asteroseismological measurements. As a development of this method, H. Jönsson et al. (2020, in preparation) have been utilizing an up to three times broader wavelength range of the high-resolution optical spectra from Jönsson et al. (2017a), Lomaeva et al. (2019), and Forsberg et al. (2019), all observed with the FIES spectrograph (Telting et al. 2014) on the Nordic Optical Telescope (NOT). In total, stellar parameters and several abundances for more than 500 K giants have been derived. We have been using a subset of these here.

The code Spectroscopy Made Easy (SME; Valenti & Piskunov 1996, 2012) is used to determine these stellar parameters. SME interpolates in a grid of one-dimensional (1D) MARCS atmosphere models (Gustafsson et al. 2008). These are hydrostatic model atmospheres in spherical geometry,

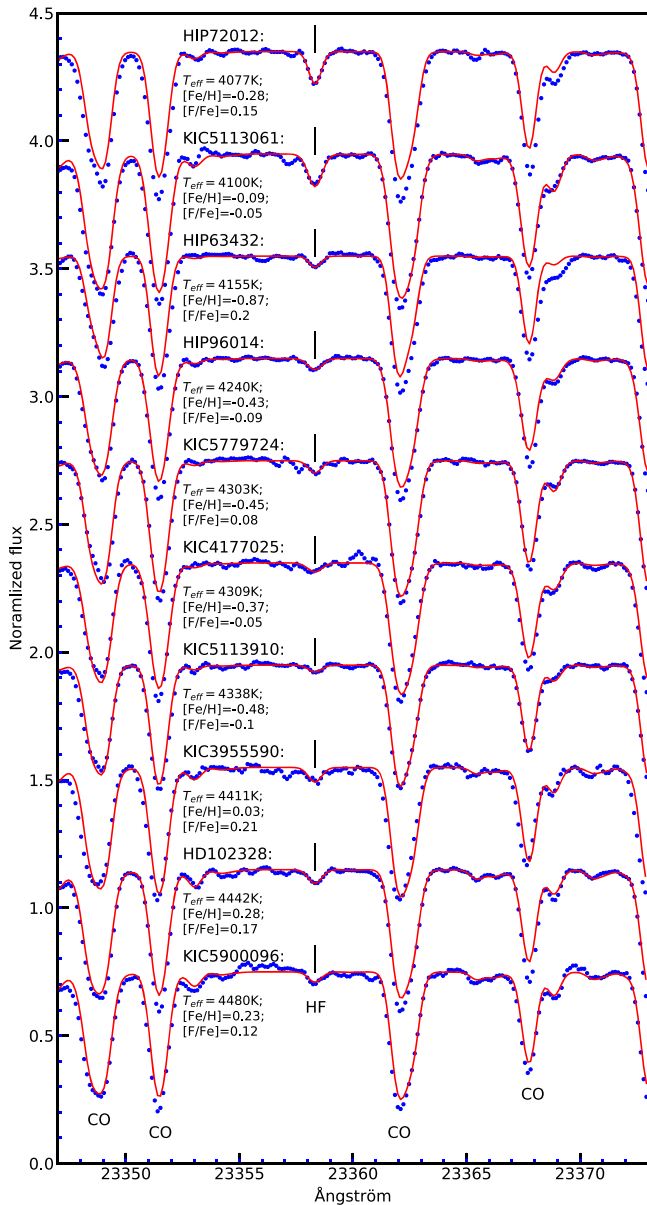


Figure 1. Observed IGRINS spectra of the 10 stars yielding a fluorine abundance. The spectra near the HF line at $\lambda_{\text{air}} = 23358.33 \text{ \AA}$, is shown with blue dotted lines. Synthetic spectra are shown by the red line. The HF line is marked with vertical lines. Only the HF line is fitted. The stars are ordered with increasing T_{eff} from the top. The other spectral lines in the figure are all CO vibration–rotational lines.

computed assuming LTE, chemical equilibrium, homogeneity, and conservation of the total flux (radiative plus convective, the convective flux being computed using the mixing-length recipe). The uncertainties achieved are $\pm 50 \text{ K}$ for T_{eff} , $\pm 0.15 \text{ dex}$ for $\log g$, $\pm 0.05 \text{ dex}$ for $[\text{Fe}/\text{H}]$, and $\pm 0.1 \text{ km s}^{-1}$ for ξ_{micro} . The final stellar parameters are given in Tables 2 and 3.

From the optical spectra, we have also determined the oxygen and cerium abundances, listed in Tables 2 and 3. The oxygen abundances were determined from the 6300.308 \AA [OI] line, and the cerium abundance from five Ce II lines between 5250 and 6050 \AA (more details in H. Jönsson et al. 2020, in preparation). These abundances are used in the trend plots in Figures 8–10.

With the derived stellar parameters, we can then synthesize spectra and determine abundances from the infrared spectra. We have chosen also here to use SME in order to be consistent with the determination of the stellar parameters, but also because it has a flexible chi-square minimization tool for finding the solution that fits an observed spectrum the best, in a prespecified spectral window. Then, we determine the fluorine abundance by fitting the HF line. To improve the rough normalization that was initially done on the spectra, a straight line was fitted to continuum regions on both sides of the HF line. Also, the width of the line, which we call ξ_{macro} and includes both the stellar macroturbulence and the spectrograph’s instrumental profile, is carefully determined as the entire line profile is fitted. For the IGRINS spectra, the ξ_{macro} is determined from a few blend-free Si lines with suitable strength for width determination, and for the narrower Phoenix spectra, the ξ_{macro} is determined from the HF features themselves and checking against the neighboring CO lines. A $\xi_{\text{macro}}^{\text{FWHM}} \sim 4.5 \text{ km s}^{-1}$ is found for all stars.

The fluorine abundance is thus determined for the 41 giants observed with the Phoenix spectrograph and the 10 giants observed with the IGRINS spectrograph that show clear HF lines. We have synthesized eight of the most promising HF lines, namely $\text{HF}(\nu = 1 - 0)$ R3, 4, 7, 9, 12, 13, 14, and 15 of the R branch. However, it is only the R9 line that can be used for an abundance determination; all the other lines have various problems, such as line blending or being too weak. Indeed, it is mostly the $\text{HF}(\nu = 1 - 0)$ R9 line that has been used in the literature.

The molecular line data, i.e., wavelengths, excitation energies, and transition probabilities ($\log gf$), are calculated and given in Jönsson et al. (2014a). These authors also stress the importance of using a partition function consistent with these excitation energies in order to get the correct abundances; otherwise, an abundance offset of ~ 0.3 dex is found. The correct partition function is given in Jönsson et al. (2014b). For such a light molecule as HF, the difference in energies is large, depending on whether the zero point of the excitation energies is set by the dissociation energy of the energy potential, D_e , or the true energy required for dissociation, D_0 . Jönsson et al. (2014a) use the latter definition. It should also be noted that there is still an uncertainty in the dissociation energy of the HF molecule, which could give an additional systematic uncertainty in the derived F abundances of $\sim 0.04 \text{ dex}$ (see discussion in Guerço et al. 2019a).

In Figure 3 of Jönsson et al. (2014a), all vibration–rotational lines in both the R and P branches are given. The P branch lines are in general stronger than the lines in the R branch, with the P10 line being the strongest. However, the P branch lies mainly between the K and L bands, where it is obscured by Earth’s atmosphere. The $\text{HF}(\nu = 1 - 0)$ P21 (and higher) lines appear in the L band ($\sim 3.5\text{--}4.1 \text{ \mu m}$).

For the 10 giants for which a Gaussian line profile could not be distinguished from the noise in the spectra, an upper limit of the fluorine abundance is determined instead. This was done such that a synthetic spectrum with an HF line clearly much stronger than the observed noise in the region of the HF line is calculated, providing an upper limit to the fluorine abundance. Five other giants that were hotter provided upper limits that were uninterestingly high and are omitted from the analysis for clarity.

Table 2
Program Stars Observed with IGRINS; Stellar Parameters and Derived Abundances on Order of T_{eff}

Star	T_{eff}	$\log g$	[Fe/H]	ξ_{micro}	$A(\text{F})$	[F/Fe]	$A(\text{O})$	[O/Fe]	[Ce/Fe]
(1)	(2)	(3)	(4)	(5)	(6)	(7)	(8)	(9)	(10)
Stars with a detected HF line:									
HIP 72012	4077	1.4	-0.28	1.5	4.30	0.15	8.58	0.17	-0.06
KIC 5113061	4100	1.7	-0.09	1.8	4.29	-0.05	8.74	0.14	-0.02
HIP 63432	4155	1.3	-0.87	1.9	3.76	0.2	8.36	0.54	-0.0
HIP 96014	4240	1.6	-0.43	1.7	3.91	-0.09	8.48	0.22	-0.05
KIC 5779724	4303	1.6	-0.45	1.7	4.06	0.08	8.74	0.50	-0.05
KIC 4177025	4309	1.7	-0.37	1.7	4.01	-0.05	8.75	0.43	-0.09
KIC 5113910	4338	1.7	-0.48	1.6	3.85	-0.10	8.46	0.25	0.08
KIC 3955590	4411	2.2	+0.03	1.6	4.67	0.21	8.89	0.17	-0.07
HD 102328	4442	2.5	+0.28	1.5	4.88	0.17	8.97	-0.01	-0.09
KIC 5900096	4480	2.5	+0.23	1.5	4.78	0.12	8.94	0.02	-0.09
Stars yielding an upper limit of the HF abundance:									
HIP 50583	4292	1.7	-0.54	1.7	<3.8	<-0.07	8.44	0.29	0.09
KIC 11045542	4304	1.6	-0.65	1.5	<3.8	<0.03	8.28	0.24	-0.01
α Boo	4308	1.7	-0.55	1.8	<3.9	<0.03	8.64	0.50	-0.13
2M14231899	4308	1.8	-0.82	1.6	<3.5	<-0.07	8.43	0.56	0.32
2M17215666	4342	1.6	-1.11	1.7	<3.5	<0.13	8.14	0.56	0.34
KIC 4659706	4428	2.5	+0.24	1.5	<4.9	<0.23	9.03	0.10	-0.04
HIP 90344	4454	2.2	-0.39	1.4	<4.3	<0.23	8.65	0.35	0.06
KIC 3936921	4488	2.2	+0.01	1.6	<4.5	<0.08	8.92	0.22	-0.11
KIC 11342694	4509	2.8	+0.14	1.3	<4.7	<0.13	8.83	0.00	-0.05
KIC 3748585	4569	2.6	+0.03	1.3	<4.6	<0.18	8.83	0.11	0.00

Note. We use $A(\text{O})_{\odot} = 8.69$ (Asplund et al. 2009), $A(\text{F})_{\odot} = 4.43$ (Lodders 2003), and $A(\text{Ce})_{\odot} = 1.58$ (Grevesse et al. 2015).

4. Results

4.1. Fluorine Abundances

The final fluorine abundances and upper limits are given in Tables 2 and 3, where we provide the number density abundances, $A(\text{F}) = \log N_{\text{F}}/N_{\text{H}} + 12$, and the $[\text{F}/\text{Fe}]$ ¹² abundance ratios. In the tables, we also provide the oxygen and cerium abundance results from the optical spectra.

In Figure 2 we present $[\text{F}/\text{H}]$ versus $[\text{Fe}/\text{H}]$ as determined from the IGRINS data (in red), the Phoenix data (in blue), and from the Jönsson et al. (2014b) TEXES determinations (in green). Upper limits are marked with triangles. In Figure 3, the $[\text{F}/\text{Fe}]$ trend is shown instead. The stellar abundances are normalized to the solar value, which is very uncertain; there is no detectable HF in the solar photosphere, so the solar abundance value is determined either from meteoritic measurements ($A_{\odot}(\text{F}) = 4.43 \pm 0.06$; Lodders 2003) or from uncertain measurements in sunspot spectra ($A_{\odot}(\text{F}) = 4.56 \pm 0.30$; Hall & Noyes 1969; Grevesse et al. 2007).¹³ More recently, Maiorca et al. (2014) analyzed a spectrum of a medium-strong sunspot umbra (~ 4250 K) determining the solar fluorine abundance of $A_{\odot}(\text{F}) = 4.40 \pm 0.25$, which is consistent with the Hall & Noyes (1969) value, with an equally large uncertainty. This nominal value is very close to the meteoritic value, but given the uncertainties in the modeling of the umbral spectra, the value to be used is the meteoritic value of Lodders (2003). It would be desirable to determine the solar fluorine abundance to a higher accuracy.

As can be seen in Table 2, only the giants with an effective temperature of less than approximately 4500 K show the HF line. For the metal-poor stars, even cooler giants are required. The method that we use for determining the stellar parameters is developed for stars warmer than approximately 4000 K, which means that we have avoided cooler stars as we aim for high accuracy and homogeneity. We realize that the HF line should get stronger for cooler stars and for stars with lower surface gravities, and these could be used for future fluorine measurements in the metal-poor region (see, e.g., the recent work by Guerço et al. 2019a). Cool, metal-poor giants are, however, very rare.

4.2. Uncertainties

Several effects could contribute to the uncertainties in the determined fluorine abundances. The uncertainties in the HF line data are very small compared to other uncertainties, at least by a factor of 10. Residuals from the telluric line division could impinge on the HF line. We have, however, checked where the telluric lines fall in all of the stars, ensuring that this is not the case. Furthermore, the way the continuum is set could affect the equivalent width of the line. We have, however, adjusted the continuum locally, minimizing this uncertainty. The largest uncertainties stem instead from the uncertainties in the stellar parameters of the stars, in spite of our efforts to determine these as accurately as possible. We have therefore allowed the stellar parameters to vary within their uncertainties. The molecular lines are very temperature sensitive, with a change in the derived fluorine of 0.1 dex for +50 K. A change of the surface gravity of 0.15 dex results in a change of the same magnitude. The uncertainties in abundance ratios are, in general, smaller as they often cancel out to various degrees. A change in the microturbulence does not affect the synthesized line, as

¹² The notation $[A/B] = \log(N_{\text{A}}/N_{\text{B}})_{*} - \log(N_{\text{A}}/N_{\text{B}})_{\odot}$, where N_{A} and N_{B} are the number abundances of elements A and B, respectively.

¹³ See also the discussion in Nault & Pilachowski (2013) about this value and a reevaluation of it due to the problems with the excitation potential of HF, now solved (Jönsson et al. 2014a).

Table 3
Program Stars Observed with the Phoenix Spectrograph at KPNO: Stellar Parameters and Derived Abundances

Star	2MASS Name	H	K (mag)	T_{eff} (mag)	$\log g$ (K)	[Fe/H] (dex)	ξ_{micro}	$A(\text{F})$ (km s^{-1})	[F/Fe]	$A(\text{O})$	[O/Fe]	[Ce/Fe]
(1)	(2)	(3)	(4)	(5)	(6)	(7)	(8)	(9)	(10)	(11)	(12)	(13)
HIP 48455	J09524585+2600248	1.3	1.2	4494	2.5	+0.27	1.5	4.98	0.28	8.88	-0.08	-0.15
HIP 68567	J14021217+4545124	3.5	3.2	4163	1.7	-0.17	1.5	4.20	-0.06	8.70	0.18	-0.11
HIP 69118	J14085485+3201083	5.2	5.0	4195	1.8	-0.17	1.5	4.27	0.01	8.72	0.2	-0.1
HIP 69316	J14111512+3217451	3.7	3.6	4475	2.6	+0.29	1.5	5.00	0.28	9.02	0.04	-0.02
HIP 70949	J14304537+0446202	2.8	2.6	4145	1.7	-0.21	1.5	4.26	0.04	8.72	0.24	0.12
HIP 72499	J14492614+1002389	4.1	4.0	4485	2.5	+0.37	1.5	5.07	0.27	8.91	-0.15	-0.14
HIP 73203	J14574158+2440267	3.7	3.5	4070	1.3	-0.52	1.6	3.97	0.06	8.64	0.47	-0.15
HIP 73917	J15062101+2626136	4.9	4.7	4204	1.8	-0.10	1.6	4.24	-0.09	8.69	0.1	-0.08
HIP 75541	J15255910+4418079	3.9	3.9	4109	1.7	-0.13	1.6	4.12	-0.18	8.71	0.15	-0.02
HIP 75572	J15261738+3420095	2.4	2.1	4014	1.3	-0.43	1.6	4.04	0.04	8.52	0.26	-0.09
HIP 75583	J15263014+2807391	4.4	4.2	4169	1.6	-0.41	1.5	3.98	-0.04	8.58	0.3	0.02
HIP 76634	J15390103+0328034	4.2	4.0	4166	2.1	+0.20	1.4	4.84	0.21	8.96	0.07	0.12
HIP 77743	J15522151+2836267	5.3	5.1	4465	2.6	+0.26	1.5	4.85	0.16	8.98	0.03	-0.1
HIP 78157	J15573375+1604218	5.8	5.7	4496	2.6	+0.33	1.5	5.10	0.34	9.02	0.	-0.02
HIP 78262	J15584908+1612399	4.5	4.3	4070	1.7	-0.05	1.5	4.39	0.01	8.80	0.16	-0.14
HIP 79120	J16085888+0327161	2.6	2.4	4106	1.8	+0.10	1.4	4.69	0.16	8.90	0.11	-0.11
HIP 79488	J16131544+0501160	2.3	2.1	4067	1.6	-0.11	1.7	4.24	-0.08	8.73	0.15	0.00
HIP 79953	J16191120+4902172	2.9	2.7	4111	1.6	-0.24	1.6	4.13	-0.06	8.62	0.17	-0.01
HIP 80693	J16283398+0039540	2.2	2.0	4115	1.8	+0.06	1.6	4.52	0.03	8.87	0.12	-0.22
HIP 82012	J16451180+4313015	3.0	2.6	4073	1.5	-0.25	1.6	4.06	-0.12	8.60	0.16	0.02
HIP 82611	J16531756+4724598	3.0	2.6	4163	1.6	-0.47	1.6	3.80	-0.16	8.54	0.32	-0.02
HIP 82802	J16552218+1825594	2.2	2.1	4086	1.7	-0.15	1.6	4.30	0.02	8.75	0.21	-0.09
HIP 83677	J17060964+0944017	3.2	2.9	4059	1.5	-0.12	1.6	4.08	-0.22	8.72	0.15	-0.03
HIP 84431	J17154147+2344338	3.2	2.8	4222	1.7	-0.09	1.6	4.34	-0.	8.72	0.12	-0.06
HIP 84659	J17182453+2656130	4.8	4.6	4356	2.0	-0.18	1.6	4.41	0.16	8.76	0.25	0.01
HIP 85109	J17233792+1323514	4.5	4.3	4314	2.2	+0.08	1.4	4.70	0.19	8.86	0.09	-0.12
HIP 85692	J17304356+5752365	3.0	2.8	4091	1.5	-0.31	1.7	3.90	-0.22	8.55	0.17	0.18
HIP 85824	J17321358+4619500	4.0	4.0	4170	1.7	-0.25	1.5	4.31	0.13	8.81	0.37	-0.03
HIP 87445	J17520472+3958553	3.0	2.8	4158	1.6	-0.26	1.6	4.06	-0.11	8.58	0.15	0.06
HIP 87777	J17555082+2227513	3.0	2.7	4383	2.1	-0.09	1.6	4.49	0.15	8.73	0.13	0.07
HIP 88770	J18072099+0228537	3.3	3.1	4050	1.5	-0.24	1.6	4.12	-0.07	8.62	0.18	-0.05
HIP 88877	J18083882+5758468	4.1	4.0	4046	1.5	-0.19	1.6	4.34	0.1	8.62	0.12	-0.1
HIP 89298	J18131656+2152493	3.0	2.8	4031	1.4	-0.29	1.5	4.19	0.05	8.59	0.19	0.03
HIP 89827	J18195206+2939588	3.3	2.9	4221	1.7	-0.17	1.6	4.24	-0.02	8.62	0.1	0.00
HIP 90915	J18324614+2337005	2.7	2.4	4008	1.5	-0.18	1.8	4.24	-0.01	8.62	0.11	0.02
HIP 92768	J18541325+2754342	2.7	2.4	4131	1.7	-0.20	1.5	4.21	-0.02	8.67	0.18	-0.07
HIP 93256	J18594548+2613492	2.2	2.0	4307	1.9	-0.31	1.4	4.23	0.11	8.56	0.18	0.01
HIP 93488	J19022156+0822248	2.7	2.5	4095	1.6	-0.22	1.8	4.04	-0.17	8.66	0.19	0.14
HIP 94591	J19145845+2823411	4.6	4.4	4181	1.6	-0.21	1.6	4.01	-0.21	8.64	0.16	0.03
HIP 96063	J19315598+3011162	4.6	4.3	4242	2.0	-0.02	1.5	4.54	0.12	8.75	0.08	-0.09
HIP 97789	J19521643+3625563	3.1	2.7	4089	1.6	-0.08	1.7	4.22	-0.13	8.71	0.1	-0.07

Note. We use $A(\text{O})_{\odot} = 8.69$ (Asplund et al. 2009), $A(\text{F})_{\odot} = 4.43$ (Lodders 2003), and $A(\text{Ce})_{\odot} = 1.58$ (Grevesse et al. 2015).

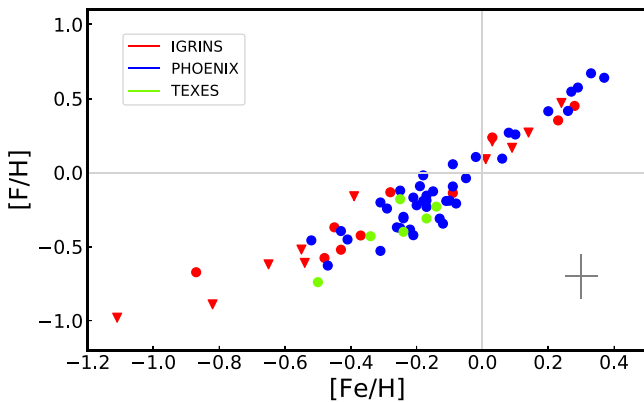


Figure 2. [F/H] as a function of metallicity, [Fe/H], is shown for the stars observed with IGRINS (red), Phoenix (blue), and TEXES (green). $A(\text{F})_{\odot} = 4.43$ (Lodders 2003).

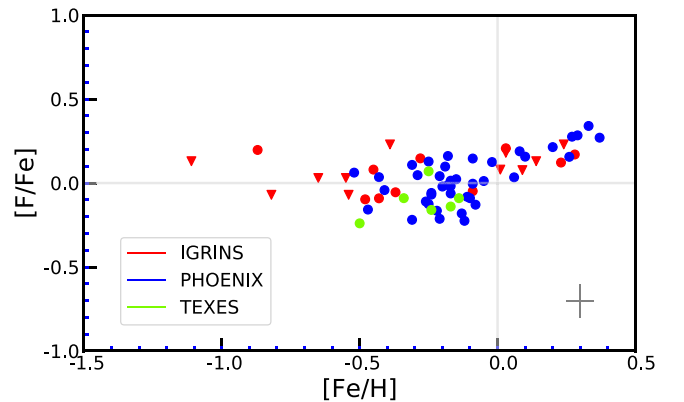


Figure 3. [F/Fe] ratio as a function of metallicity is shown for the stars observed with IGRINS (red), Phoenix (blue), and TEXES (green). $A(\text{F})_{\odot} = 4.43$ (Lodders 2003).

expected for these weak lines. This shows that it is important to determine the T_{eff} and $\log g$ very well in order to minimize the scatter in the fluorine trends with metallicity. We estimate a total uncertainty in the derived fluorine abundances to be $\sigma_A(\text{F}) \sim 0.15$ dex and in the abundance ratios to be $\sigma([\text{F}/\text{Fe}]) \sim 0.10$ dex.

The robustness of our method is demonstrated by the similarity between our abundance trends derived from the two different spectrographs (IGRINS and Phoenix) and that determined from the TEXES spectrograph, showing the similarity of the abundances derived from the two diagnostics (the vibration–rotational lines at $2.3 \mu\text{m}$ and the pure rotational lines at $12 \mu\text{m}$).

5. Discussion

5.1. Nucleosynthesis of Fluorine

In the following, a short overview of the possible production sites of fluorine that may be important and are discussed theoretically is given. The predicted trends from the different channels are discussed, which will be important when analyzing our data later on.

(i) The contributions to the cosmic budget of fluorine from nonrotating massive stars and conventional Type II supernovae are negligible (Kobayashi et al. 2011b; Prantzos et al. 2018). Rapidly rotating massive stars can, however, produce primary fluorine from ^{14}N , via proton and α captures in the presence of ^{13}C , which is needed for the generation of protons (Prantzos et al. 2018). The ^{14}N comes from reactions with ^{12}C which is the ashes of He burning in the massive star itself and is therefore of primary origin (Guerço et al. 2019a). This process could dominate the F budget all the way up to solar metallicities.

(ii) The ν process, active during core-collapse supernovae (Woosley & Haxton 1988; Woosley et al. 1990; Timmes et al. 1995; Langanke et al. 2019), could contribute substantially to the fluorine production (Kobayashi et al. 2011a; Nault & Pilachowski 2013; Pilachowski & Pace 2015). In this process, fluorine is formed from neutrino-induced spallation reactions with ^{20}Ne in the expelled shell, containing nuclei formed in the progenitor star. Fluorine is then a primary element, formed from a process that is independent of the metallicity of the site of formation. Because the progenitor stars are massive, short-lived stars, they contribute early (Olive & Vangioni 2019), already at low metallicities, and at a constant ratio with oxygen, another element synthesized in massive stars ending their lives as Type II supernovae. However, there are still large uncertainties in the stellar modeling (such as progenitor mass and distribution of ^{20}Ne) and the neutrino-induced thermonuclear reaction rates of ^{20}Ne (Sieverding et al. 2018, 2019). The F production is also very sensitive to the modeled neutrino flux and its spectrum (Alibés et al. 2001; Prantzos et al. 2018; Langanke et al. 2019; Olive & Vangioni 2019).

(iii) During the He-burning thermal pulses (TP) in AGB stars, the ^{14}N produced in the hydrogen-burning CNO cycle can produce fluorine through a chain of reactions also involving neutrons and protons, a process discussed by, for example, Forestini et al. (1992), Jorissen et al. (1992), Abia et al. (2011), and Cristallo et al. (2014). Subsequently, the star undergoes the third dredge-up, during which the surface is enriched with fluorine. This fluorine is subsequently expelled to the interstellar medium by stellar winds and/or during the

planetary nebula phase of the star. Fluorine produced through this channel would be a secondary element (Prantzos et al. 2018), with yields depending on the metallicity of the star forming it. Goriely & Mowlavi (2000) also show the importance of partial mixing of protons into the carbon-rich layers in the interiors of AGB stars during the third dredge-up, for the formation of fluorine.

At too high temperatures in the stellar interiors, helium-nuclei or proton-capture reactions destroy fluorine, converting it to Ne, as mentioned above. Therefore, the AGB stars that form fluorine are less massive than approximately $4 M_{\odot}$, preventing the high temperatures of hot bottom burning (Kobayashi et al. 2011a). The fluorine production in AGB stars is, indeed, mass dependent between 2 and $4 M_{\odot}$, with a maximum around $3 M_{\odot}$ (Kobayashi et al. 2011b). Due to the time delay for low- and intermediate-mass stars to start contributing to the cosmic buildup of fluorine, this source will start contributing at a higher metallicity ($[\text{Fe}/\text{H}] \sim -0.9$ to -0.7 Kobayashi et al. 2011a) and will be different for different stellar populations with different star formation rates. This process was observationally argued to be a dominant source of present-day cosmic fluorine in the solar neighborhood by, for example, Jorissen et al. (1992), Recio-Blanco et al. (2012), Jönsson et al. (2014b), Olive & Vangioni (2019), Guerço et al. (2019a), and Abia et al. (2015a, 2015b). The last also concludes that additional sources are necessary. Abia et al. (2019) argue that AGB stars do contribute, not as the main source in the solar neighborhood, however, and thus contrary to Olive & Vangioni (2019), among others.

(iv) A similar reaction chain could occur in massive Wolf–Rayet stars, a process investigated early on by Meynet & Arnould (2000) and discussed and argued for in, e.g., Cunha et al. (2003), Renda et al. (2004), Cunha et al. (2008), and Spitoni et al. (2018), but questioned in Palacios et al. (2005) when rotation is included. ^{14}N , also here resulting from the CNO cycle as a secondary element (N formed from the preexisting C), is converted to fluorine during the core-helium-burning phase, and subsequently expelled through the strong, metal-line driven wind. In this channel, the fluorine produced therefore acts as a secondary element, at high enough metallicities. The formation of Wolf–Rayet stars and their winds is also metallicity dependent, thus becoming increasingly important first for higher metallicities (Cunha et al. 2003) and should, therefore, be less dependent on the star formation rates of different stellar populations. Primary nitrogen, subsequently burning to fluorine, can also be produced, but is restricted to metal-poor, rotating massive stars (Meynet & Maeder 2002; Spitoni et al. 2018).

It should, however, be noted that the conditions and mechanisms in Wolf–Rayet stars for fluorine to survive and contribute to the cosmic F reservoir are very uncertain; recent massive-star models with mass-loss rates accounting for the reduction factor due to clumping show that these stars might not at all be significant as a source of cosmic fluorine (G. Meynet 2020, private communication). This was also shown earlier by Palacios et al. (2005).

(v) Spitoni et al. (2018) discuss the possibility of novae contributing to the cosmic budget of fluorine. These could, in principle, produce fluorine (José & Hernanz 1998) through reactions starting with proton captures by ^{17}O nuclei. Indeed, Spitoni et al. (2018) conclude that this process might be important to reproduce the secondary behavior of the observed

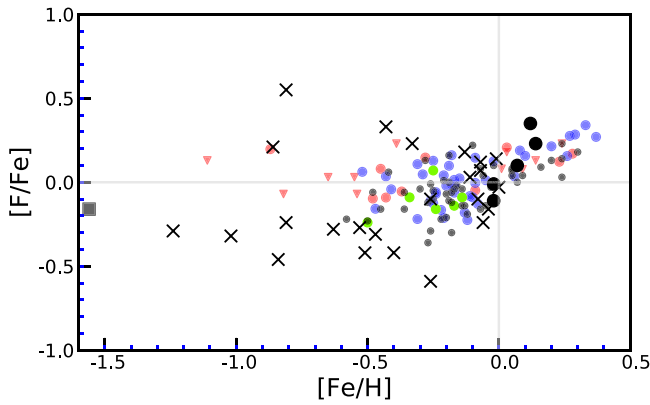


Figure 4. $[F/Fe]$ vs. $[Fe/H]$ compared to determinations from the literature. Large black dots are from Nault & Pilachowski (2013), small gray dots from Jönsson et al. (2017b), the square from Li et al. (2013), and crosses from Guerço et al. (2019a), with the two metal-poor stars with high $[F/Fe]$ probably being members of the Monoceros overdensity (Guerço et al. 2019a).

fluorine trends. It should also be noted that the novae yields are also highly uncertain (Spitoni et al. 2018).

5.2. Fluorine Abundances and Ratios versus Metallicity

The abundances as a function of metallicity, presented in Figure 2, show a very tight relation, close to linear. At lower metallicities, these abundance ratios might decrease more slowly as the metallicity decreases. The spread in the F abundances in the range between $[Fe/H] \sim -0.6$ up to solar metallicity is larger than that for supersolar metallicities. This is even more evident in Figure 3, where $[F/Fe]$ is plotted versus metallicity. Below $[Fe/H] \sim -0.6$, we have three upper limits and one determined abundance from a clearly detected HF line in the spectrum of the giant HIP 63432, with $[Fe/H] = -0.87$. This spectrum is displayed in Figure 1 and has a $[F/Fe] = 0.2$. Note that our estimated uncertainties, mainly due to the uncertainties in the stellar parameters, is of the order of $\sigma[F/Fe] \sim 0.1$ dex. This low-metallicity trend with metallicity seems, thus, to be quite flat, with indications of a detectable spread. However, more fluorine determinations in metal-poor stars are clearly needed.

All trends go roughly through the expected solar values, $([F/Fe], [Fe/H]) = (0, 0)$. It should, however, be kept in mind that the solar F-abundance determinations are subjected to large uncertainties (of the order of ± 0.25 dex; Hall & Noyes 1969; Grevesse et al. 2007; Maiorca et al. 2014) and that we are using the meteoric value of Lodders (2003). The choice of the value of the solar fluorine abundance only results in a scaling of the abundances in the figures, but should be taken into account for comparisons with other published abundances.

Our abundances show less scatter in the trends than many previous investigations (see, e.g. Recio-Blanco et al. 2012; Pilachowski & Pace 2015; Jönsson et al. 2017b). For the narrow metallicity range of the open cluster giants in Nault & Pilachowski (2013), our results agree very well, with a clear increase at supersolar values; see Figure 4. Furthermore, our new abundances based on the Phoenix spectra show a slightly smaller scatter, and a tighter correlation, than those determined by Jönsson et al. (2017b), who analyzed the same spectra (see the small gray dots in Figure 4). We believe the reason for this smaller scatter is caused by our more accurate stellar parameters. Also, the trends discussed in Guerço et al. (2019a) agree very well with ours (crosses in Figure 4), within

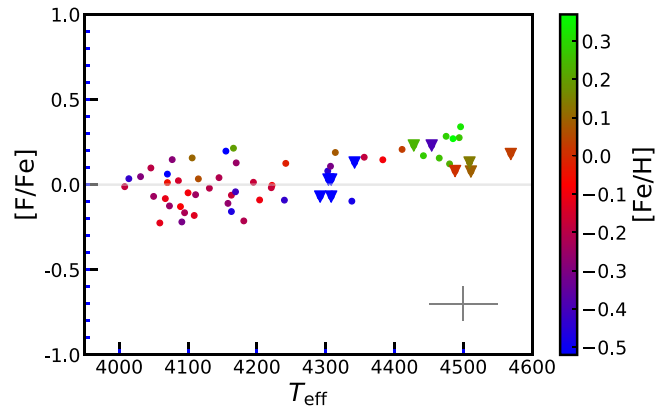


Figure 5. $[F/Fe]$ as a function of effective temperature, color-coded for the stars' metallicities, $[Fe/H]$.

the common metallicity range. In light of their plateau suggested by the data of Guerço et al. (2019a) at low metallicities ($[Fe/H] < -0.5$; excluding the probable members of the Monoceros overdensity) and the data point from the study of Li et al. (2013), our indications of a plateau is strengthened. The plateau in Guerço et al. (2019a), however, lies at a ~ 0.2 dex lower level.

In Figure 5, we plot the $[F/Fe]$ abundance ratios as a function of effective temperature, color-coding the stars for their metallicities. Stars cooler than approximately 4350 K show no trend with T_{eff} but a scatter. For the warmer stars, only higher $[F/Fe]$ values are measured, tracing the upper range of the scatter. This effect is also seen and discussed in Pilachowski & Pace (2015). In the warmer stars, the HF line increasingly disappears, and only the stars with a high F abundance will be detected. Lower abundance, such as for metal-poor stars, will not yield a strong-enough HF line to be detected for the warm stars. Indeed, among the warmer stars, we find mostly metal-rich stars, for which we see an upturn in $[F/Fe]$ in Figure 3. Furthermore, few metal-poor stars are found at temperatures above 4350 K.

In Figure 6, we plot the $[F/Fe]$ abundance ratios instead, as a function of metallicity, color-coding the stars for their effective temperatures. No trend with T_{eff} is detected, apart from the most metal-rich stars being predominately warm. The reason for this is seen in the Kiel diagram in the lower-left corner of the figure. There, we clearly see the giant branch with the metallicities increasing diagonally to lower temperatures, as expected (see also Jönsson et al. 2017a). Most of our warm stars above 4400 K are red clump stars and are metal rich. Note that some of the high-metallicity stars are also cooler. Had we targeted more stars, we would have detected the HF line in a larger number of cooler stars. The line is actually more easily detected the cooler the giant star is, due to the molecular equilibrium. However, the lower number of warm, metal-poor stars in the Kiel diagram is caused by the HF line strength becoming weaker and eventually disappearing.

5.3. Thin- and Thick-disk Trends

In Figure 7, we again plot the $[F/Fe]$ ratios as a function of metallicity, but this time color-coding the stars according to the assigned stellar population, i.e., thin-disk, thick-disk, or halo stars as determined from the separation in the $[Mg/Fe]$ versus $[Fe/H]$ plane (see H. Jönsson et al. 2020, in preparation for details). If anything, there is a slight tendency that the thick-

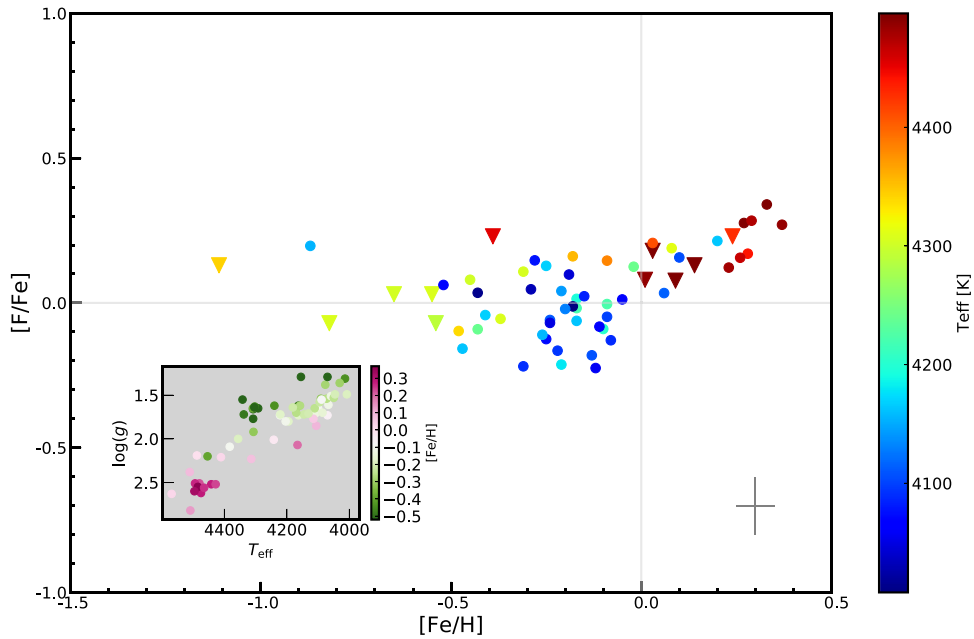


Figure 6. $[F/Fe]$ as a function of $[Fe/H]$ color-coded for the stars’ effective temperatures, T_{eff} . The figure in the lower left corner is a Kiel diagram for the same stars color-coded for their metallicities.

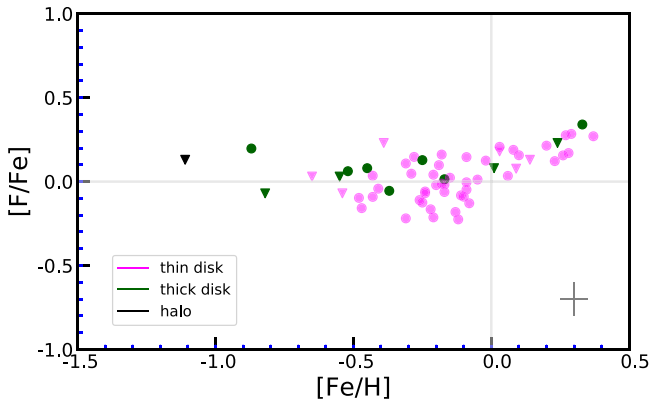


Figure 7. $[F/Fe]$ as a function of $[Fe/H]$ for the stars analyzed here, color-coded based on their assigned stellar population, i.e., thin-disk, thick-disk, or halo stars as determined from the separation in the $[Mg/Fe]$ vs. $[Fe/H]$ plane (see H. Jönsson et al. 2020, in preparation for details).

disk stars seem to lie at the upper envelope of the thin-disk stars. More data are needed to confirm this observation. This is, however, theoretically expected according to the models in Kobayashi et al. (2011a, 2011b), also plotted in Jönsson et al. (2017b). We have also been able to determine an upper limit of the F abundance for the only halo star in our sample, which is, on the other hand, much lower than what is predicted in Kobayashi et al. (2011b).

5.4. Secondary-element Behavior

Another way to investigate the importance of the different nucleosynthetic processes for the cosmic fluorine budget is to look for the signatures of fluorine’s primary or secondary origin; see Section 5.1. Because oxygen is produced as a primary element in massive stars (see, e.g., Prantzos et al. 2018), plotting the number density of fluorine as a function of the number density of oxygen will reveal whether fluorine is primary or whether it behaves like a secondary element. In Figure 8, we plot $A(F)$ versus $A(O)$. A linear regression gives a

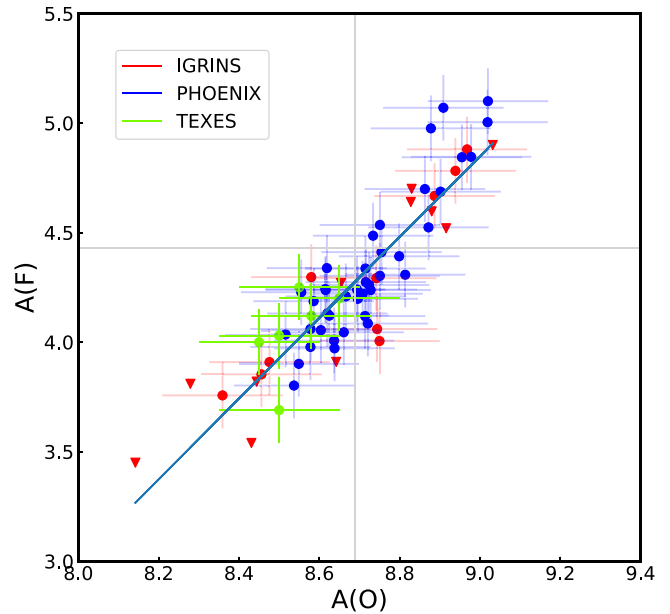


Figure 8. Number density of fluorine as a function of the number density of oxygen for the stars analyzed here (red and blue) and those from Jönsson et al. (2014b) from their $12\ \mu\text{m}$ observations (green). Typical error bars are marked. The blue straight line is a linear regression to the data with a slope of 1.8, which is close to 2.

slope of 1.8 ± 0.2 , which is a clear indication of a secondary behavior. One can also directly plot the fluorine-to-oxygen abundance ratio as a function of the oxygen abundance, which will be a constant for a primary element and give a slope of one for a secondary element. In Figure 9, this is plotted and we can reject the hypothesis of a primary element as the trend is not constant. The slope is instead close to one, 1 ± 0.2 , which is the signature of a secondary element.

The synthesis of fluorine in evolved red giant stars has been demonstrated observationally by a number of studies, beginning with that of Jorissen et al. (1992) and more recently those

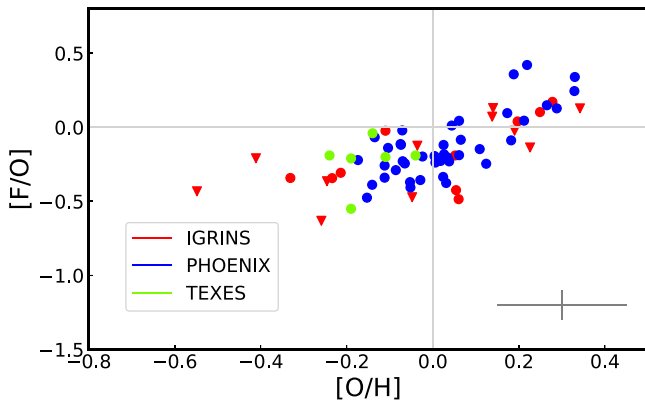


Figure 9. Fluorine-to-oxygen ratio vs. the oxygen abundance for the three sets of stars.

of, e.g., Pandey (2006), Alves-Brito et al. (2011), Lucatello et al. (2011), and Abia et al. (2015a, 2019). This is the only nucleosynthetic process forming fluorine that has an observational proof of its activity. From several papers on the galactic chemical evolution of fluorine, the AGB-star contribution in the approximate metallicity range of $-0.6 < [\text{Fe}/\text{H}] < 0.0$ is, indeed, claimed to be dominant (e.g., Renda et al. 2004; Recio-Blanco et al. 2012; Spitoni et al. 2018; Olive & Vangioni 2019). It should, however, be noted that there are different theoretical predictions of the AGB-star contributions, mainly due to which nuclear reaction rates are adopted. For instance, Prantzos et al. (2018) find a lower AGB stellar yield than Kobayashi et al. (2011b) or Spitoni et al. (2018); see also the discussion in Guerço et al. (2019a).

Due to the time delay of the AGB stars producing cosmic fluorine, their contribution is theoretically predicted to start contributing at metallicities larger than $[\text{Fe}/\text{H}] \sim -0.9$ for the thin disk and at $[\text{Fe}/\text{H}] \sim -0.7$ for the thick disk (see Kobayashi et al. 2011a, 2011b; Spitoni et al. 2018). Thus, with these theoretical predictions and our observationally determined secondary behavior, we conclude that the AGB-star contribution must be dominant at least in the $-0.6 < [\text{Fe}/\text{H}] < 0.0$ range, thus corroborating the findings of Recio-Blanco et al. (2012), Jönsson et al. (2017b), Olive & Vangioni (2019), and Guerço et al. (2019a). The AGB contribution would also naturally cause the large spread in the $[\text{F}/\text{Fe}]$ versus $[\text{Fe}/\text{H}]$ plot, which we see in our data, due to the range in masses (and therefore time delays) contributing.

For high metallicities, above solar, we find an increasing $[\text{F}/\text{Fe}]$ trend displaying only a small scatter. This part also shows a secondary behavior. The large increasing trend is surprising, because according to galactic chemical evolution models, like the ones in Spitoni et al. (2018), the Fe contribution from Type Ia supernovae should nominally decrease the trend. The yields needed to increase it instead are larger than the current best description of the yields from Wolf-Rayet stars and novae (Spitoni et al. 2018), which are, most likely, even over-estimated. In order to fit the increasing abundances at high metallicities, Spitoni et al. (2018) tried to model the galactic chemical evolution of fluorine by artificially increasing the Wolf-Rayet yields as well as including a fluorine production from novae, which could better model the observed data. Thus, the supersolar fluorine trend can currently not be explained theoretically.

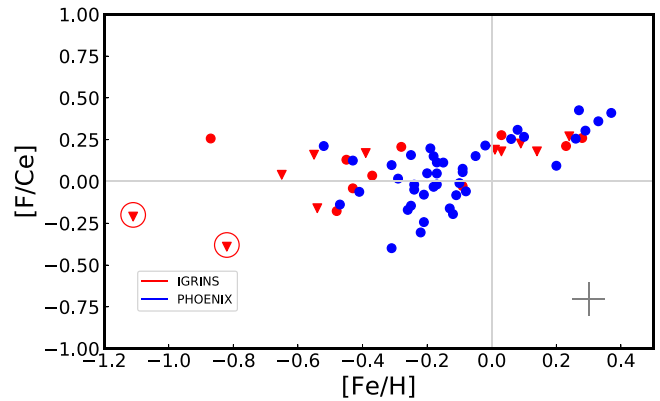


Figure 10. Ratio of fluorine to the s -process element Ce which, in general, shows quite a flat trend for subsolar metallicities. The two giants enhanced in s -process elements are marked with red circles. These have values lower than the expected trend, caused by the high Ce abundances for normal F abundances (upper limits in these cases). The Ce and F abundances are, thus, not enhanced simultaneously in these two stars. We use the solar Ce abundance from Grevesse et al. (2015): $A(\text{Ce})_{\odot} = 1.58$.

5.5. The Metal-poor Region

Unfortunately, we do not have many stars in the metal-poor region. We have, however, one robust detection at $[\text{Fe}/\text{H}] = -0.87$, which shows a supersolar $[\text{F}/\text{Fe}]$ value of $+0.2 \pm 0.1$. This, together with our upper limits, and in light of the work by Guerço et al. (2019a) and Li et al. (2013), we cannot reject a (primary) contribution at early times. The AGB-star contribution is much too low at these metallicities. The models predicting a primary contribution at low metallicities are (i) the rapidly rotating, massive-star channel (Prantzos et al. 2018) and (ii) the ν process channel (most recently; Olive & Vangioni 2019). The trend from the rotating massive stars is a shallow and slightly larger-than-solar $[\text{F}/\text{Fe}]$ for all metallicities (Prantzos et al. 2018), which is in better agreement with our data than the ν process prediction, which is lower for all metallicities.

5.6. Stars Enriched in s -process Elements

The main s -process takes place in the interior of low- and intermediate-mass AGB stars (see, e.g., the discussion in Forsberg et al. 2019), and Ce is to 84% a main s -process element (Bisterzo et al. 2014). The $[\text{F}/\text{Ce}]$ ratio should then be constant for the interval in metallicities where both elements are predominantly synthesized by the same type of AGB stars. We show the $[\text{F}/\text{Ce}]$ ratio as a function of metallicity in Figure 10. Apart from the supersolar metallicities, the ratio is almost flat, although with some scatter. This strengthens the conclusion that AGB stars could be the dominant source of fluorine at least in the $-0.6 < [\text{Fe}/\text{H}] < 0.0$ range.

In the full sample of stars from which we have chosen our subset of stars, there are a number of stars that are enriched in s -process elements. These stars are significantly enriched in Zr, La, and Ce, simultaneously and by the same amount. The origin of these stars and the cause of this enrichment is not known, but being K giants, one possibility could be that the stars are in binary systems, i.e., they are extrinsic s -enhanced stars. The s -process element enhancement is then probably caused by pollution from the evolved AGB companion. This enhancement should then be accompanied by a fluorine enhancement, as fluorine is expected to correlate with the s -process elements, because both production chains include

neutrons coming from He-nuclei reactions with ^{13}C (Abia et al. 2019). In solar-metallicity carbon stars (on the AGB), this is indeed observed (Goriely & Mowlavi 2000; Abia et al. 2019). It would, therefore, be interesting to investigate whether these stars are enhanced in fluorine too.

We have determined upper limits of the fluorine abundances for two of these stars enhanced in *s*-process elements (2M14231899 and 2M17215666), both below $[\text{F}/\text{H}] < -0.8$, one being a thick disk and one a halo star. In Figures 2 and 3, we see that the upper limits for these stars are not especially high. On the contrary, they are even smaller than the robustly determined fluorine abundance from the star with a metallicity intermediate between the two stars. Thus, the fluorine abundances do not seem abnormally high, although we have very few data points in this metallicity range. The $[\text{F}/\text{Ce}]$ ratio as a function of metallicity is plotted in Figure 10. The high Ce abundance and the normal fluorine abundances put these two stars below the general flat trend, and especially below the ratio of the star with the intermediate metallicity. We thus conclude that these *s*-enhanced stars do not show abnormally high fluorine abundances. This is surprising because it might have been expected had these elements originated from AGB stars.

We checked for binarity for these stars by looking for radial velocity shifts in spectra observed by APOGEE (SDSS IV; Majewski et al. 2017; Holtzman et al. 2018) at different epochs, but could not find any sign of binarity. Thus, the argument for them being extrinsic *s*-enhanced stars is weakened. Another possibility may be that they are globular-cluster escapees, which could leave traces of enrichment from AGB stars, and therefore the enhancement of the *s*-process elements. But then, fluorine enhancements could possibly also be expected.

It therefore seems unlikely that AGB stars, at these metallicities, are the cause of the *s*-process element enhancement or that fluorine is not produced at the same enhancement levels as the *s*-process elements from AGB stars. At these metallicities, the *s*-process elements could also have contributions from the *r*-process, which does not produce fluorine. The fluorine would then be produced in rapidly rotating massive stars or through the ν process.

We note that Cunha et al. (2003) also found that in their measurements of stars in ω Cen, stars with enhancements of *s*-process elements at similar metallicities, revealing a large contribution of AGB stars to the chemical evolution, did not show enhanced levels of fluorine either. These arguments strengthen the non-AGB contribution at lower metallicities. We also note, however, that Abia et al. (2019) conclude from analyzing carbon-rich AGB stars of different metallicities that models overpredict the production of fluorine for metal-poor stars ($[\text{Fe}/\text{H}] < -0.5$), which could potentially explain a lower F abundance than expected. It would be very interesting to measure the fluorine abundances in the other *s*-process-enriched stars from H. Jönsson et al. (2020, in preparation), which are at higher metallicities, in a range where the AGB-star contribution is high.

We can thus corroborate the results in Guerço et al. (2019a), who argue for a primary behavior at $[\text{Fe}/\text{H}] < -0.5$ and a secondary behavior above -0.5 . This is supported by the fact that the *s*-enhanced stars in our sample do not show enhanced F for metallicities lower than $[\text{Fe}/\text{H}] < -0.6$.

6. Conclusions

With the aim of putting constraints on the cosmic origin of fluorine, we have derived the fluorine abundances in 61 K giants in the solar neighborhood with $-1.1 < [\text{Fe}/\text{H}] < +0.4$ by analyzing the $2.3\ \mu\text{m}$ HF line. Apart from the Phoenix spectra from Jönsson et al. (2017b), we present new spectra observed with the IGRINS spectrograph at high spectral resolution. In order to minimize the scatter in the data, we have carefully determined accurate stellar parameters in a homogeneous way for all these stars.

We find, in principle, a flat $[\text{F}/\text{Fe}]$ versus $[\text{Fe}/\text{H}]$ trend for subsolar metallicities, but an increasing trend above solar metallicities. This increase in $[\text{F}/\text{Fe}]$ is difficult to explain; even if possible, novae and the less likely Wolf–Rayet channels are at play for these metallicities, and the predicted fluorine production is not enough (Spitoni et al. 2018).

We also find a clear secondary behavior for our stars. In the $-0.6 < [\text{Fe}/\text{H}] < 0$ range, this secondary behavior, together with the flat $[\text{Ce}/\text{F}]$ trend, and the theoretically predicted importance of the processes in AGB stars forming cosmic fluorine, leads us to the conclusion that this channel dominates in this metallicity range.

Furthermore, together with the finding that two metal-poor, *s*-process element-rich stars do not show an enhanced fluorine abundance, and as both fluorine from AGB stars and Fe from Type Ia supernovae are time delayed (which for the thick disk means after $[\text{Fe}/\text{H}] \sim -0.7$), we cannot reject the hypothesis that for $[\text{Fe}/\text{H}] < -0.7$, the fluorine originates from massive stars, most likely from processes in rapidly rotating massive stars (Prantzos et al. 2018; Guerço et al. 2019a; Olive & Vangioni 2019), showing a primary behavior.

Therefore, it seems likely that several channels are needed to explain the cosmic budget of fluorine at different metallicities, corroborating the discussions in Abia et al. (2015a) and Cunha et al. (2008). Renda et al. (2004) also showed that different contributions are needed. They showed that the ν process could be dominant at low metallicities, that the significance of the AGB stars successively grows, and that the contribution of Wolf–Rayet stars is significant for solar and supersolar metallicities. This was also shown by Spitoni et al. (2018). It should, however, be noted that newer models might weaken the case for the Wolf–Rayet channel. Olive & Vangioni (2019) also argue that several processes are needed, with the ν process being important at early times and that the AGB contribution is the major one at solar metallicities.

It is clear that further observations and measurements of the cosmic fluorine trend at low metallicities are needed. The causes of the increasing $[\text{F}/\text{Fe}]$ ratios for supersolar metallicities also require further theoretical considerations.

We would like to thank George Meynet for fruitful and enlightening discussions on massive-star yields and the theoretically predicted role of Wolf–Rayet stars for the production of fluorine. N.R. acknowledges support from the Swedish Research Council, V.R. (project numbers 621-2014-5640), and the Royal Physiographic Society in Lund through the Stiftelse Walter Gyllenbergs fond and Märta och Erik Holmbergs donation. H.J. acknowledges support from the Crafoord Foundation, Stiftelsen Olle Engkvist Byggmästare, and Ruth och Nils-Erik Stenbäcks stiftelse. This work used the Immersion Grating Infrared spectrograph (IGRINS) that was developed under a collaboration between the University of

Texas at Austin and the Korea Astronomy and Space Science Institute (KASI) with the financial support of the US National Science Foundation under grants AST-1229522 and AST-1702267, of the McDonald Observatory of the University of Texas at Austin, and of the Korean GMT Project of KASI.

Facilities: McDonald Observatory (IGRINS), Lowell Observatory (IGRINS), KPNO (Phoenix).

ORCID iDs

Nils Ryde  <https://orcid.org/0000-0001-6294-3790>
 Henrik Jönsson  <https://orcid.org/0000-0002-4912-8609>
 Gregory Mace  <https://orcid.org/0000-0001-7875-6391>
 Katia Cunha  <https://orcid.org/0000-0001-6476-0576>
 Emanuele Spitoni  <https://orcid.org/0000-0001-9715-5727>
 Melike Afşar  <https://orcid.org/0000-0002-2516-1949>
 Daniel Jaffe  <https://orcid.org/0000-0003-3577-3540>
 Rebecca Forsberg  <https://orcid.org/0000-0001-6079-8630>
 Kyle F. Kaplan  <https://orcid.org/0000-0001-6909-3856>
 Benjamin T. Kidder  <https://orcid.org/0000-0002-2039-7143>
 Jae-Joon Lee  <https://orcid.org/0000-0003-0894-7824>
 Heeyoung Oh  <https://orcid.org/0000-0002-0418-5335>
 Verne V. Smith  <https://orcid.org/0000-0002-0134-2024>
 Christopher Sneden  <https://orcid.org/0000-0002-3456-5929>
 Kimberly R. Sokal  <https://orcid.org/0000-0002-3621-1155>
 Brian Thorsbro  <https://orcid.org/0000-0002-5633-4400>

References

- Abia, C., Cristallo, S., Cunha, K., de Laverny, P., & Smith, V. V. 2019, *A&A*, **625**, A40
- Abia, C., Cunha, K., Cristallo, S., et al. 2011, *ApJL*, **737**, L8
- Abia, C., Cunha, K., Cristallo, S., & de Laverny, P. 2015a, *A&A*, **581**, A88
- Abia, C., Cunha, K., Cristallo, S., & de Laverny, P. 2015b, *A&A*, **584**, C1
- Alibés, A., Labay, J., & Canal, R. 2001, *A&A*, **370**, 1103
- Alves-Brito, A., Karakas, A. I., Yong, D., Meléndez, J., & Vásquez, S. 2011, *A&A*, **536**, A40
- Asplund, M., Grevesse, N., Sauval, A. J., & Scott, P. 2009, *ARA&A*, **47**, 481
- Bisterzo, S., Travaglio, C., Gallino, R., Wiescher, M., & Käppeler, F. 2014, *ApJ*, **787**, 10
- Cristallo, S., Di Leva, A., Imbriani, G., et al. 2014, *A&A*, **570**, A46
- Cunha, K., Smith, V. V., & Gibson, B. K. 2008, *ApJ*, **679**, L17
- Cunha, K., Smith, V. V., Lambert, D. L., & Hinkle, K. H. 2003, *AJ*, **126**, 1305
- de Laverny, P., & Recio-Blanco, A. 2013, *A&A*, **560**, A74
- Forestini, M., Goriely, S., Jorissen, A., & Arnould, M. 1992, *A&A*, **261**, 157
- Forsberg, R., Jönsson, H., Ryde, N., & Matteucci, F. 2019, *A&A*, **631**, A113
- Goriely, S., & Mowlavi, N. 2000, *A&A*, **362**, 599
- Grevesse, N., Asplund, M., & Sauval, A. J. 2007, *SSRv*, **130**, 105
- Grevesse, N., Scott, P., Asplund, M., & Sauval, A. J. 2015, *A&A*, **573**, A27
- Guerço, R., Cunha, K., Smith, V. V., et al. 2019a, *ApJ*, **885**, 139
- Guerço, R., Cunha, K., Smith, V. V., et al. 2019b, *ApJ*, **876**, 43
- Gustafsson, B., Edvardsson, B., Eriksson, K., et al. 2008, *A&A*, **486**, 951
- Hall, D. N. B., & Noyes, R. W. 1969, *ApL*, **4**, 143
- Hinkle, K. H., Blum, R. D., Joyce, R. R., et al. 2003, *Proc. SPIE*, **4834**, 353
- Hinkle, K. H., Cuberly, R. W., Gaughan, N. A., et al. 1998, *SPIE*, **3354**, 810
- Holtzman, J. A., Hasselquist, S., Shetrone, M., et al. 2018, *AJ*, **156**, 125
- Jönsson, H., Ryde, N., Harper, G. M., et al. 2014a, *A&A*, **564**, A122
- Jönsson, H., Ryde, N., Harper, G. M., Richter, M. J., & Hinkle, K. H. 2014b, *ApJL*, **789**, L41
- Jönsson, H., Ryde, N., Nordlander, T., et al. 2017a, *A&A*, **598**, A100
- Jönsson, H., Ryde, N., Spitoni, E., et al. 2017b, *ApJ*, **835**, 50
- Jorissen, A., Smith, V. V., & Lambert, D. L. 1992, *A&A*, **261**, 164
- José, J., & Hernanz, M. 1998, *ApJ*, **494**, 680
- Kobayashi, C., Izutani, N., Karakas, A. I., et al. 2011a, *ApJL*, **739**, L57
- Kobayashi, C., Karakas, A. I., & Umeda, H. 2011b, *MNRAS*, **414**, 3231
- Lacy, J. H., Richter, M. J., Greathouse, T. K., Jaffe, D. T., & Zhu, Q. 2002, *PASP*, **114**, 153
- Langanke, K., Martínez-Pinedo, G., & Sieverding, A. 2019, arXiv:1901.03741
- Lee, J.-J., Gullikson, K., & Kaplan, K. 2017, *Igrins/Plp 2.2.0*, Zenodo, 10.5281/zenodo.845059
- Li, H. N., Ludwig, H. G., Caffau, E., Christlieb, N., & Zhao, G. 2013, *ApJ*, **765**, 51
- Lodders, K. 2003, *ApJ*, **591**, 1220
- Lomaeva, M., Jönsson, H., Ryde, N., Schultheis, M., & Thorsbro, B. 2019, *A&A*, **625**, A141
- Lucatello, S., Masseron, T., Johnson, J. A., Pignatari, M., & Herwig, F. 2011, *ApJ*, **729**, 40
- Mace, G., Kim, H., Jaffe, D. T., et al. 2016, *Proc. SPIE*, **9908**, 99080C
- Mace, G., Sokal, K., Lee, J.-J., et al. 2018, *Proc. SPIE*, **10702**, 107020Q
- Maiorca, E., Uitenbroek, H., Uttenthaler, S., et al. 2014, *ApJ*, **788**, 149
- Majewski, S. R., Schiavon, R. P., Frinchaboy, P. M., et al. 2017, *AJ*, **154**, 94
- Meynet, G., & Arnould, M. 2000, *A&A*, **355**, 176
- Meynet, G., & Maeder, A. 2002, *A&A*, **390**, 561
- Nault, K. A., & Pilachowski, C. A. 2013, *AJ*, **146**, 153
- Olive, K., & Vangioni, E. 2019, *MNRAS*, **490**, 4307
- Palacios, A., Arnould, M., & Meynet, G. 2005, *A&A*, **443**, 243
- Pandey, G. 2006, *ApJL*, **648**, L143
- Pandey, G., Lambert, D. L., & Kameswara Rao, N. 2008, *ApJ*, **674**, 1068
- Park, C., Jaffe, D. T., Yuk, I.-S., et al. 2014, *Proc. SPIE*, **9147**, 91471D
- Pilachowski, C. A., & Pace, C. 2015, *AJ*, **150**, 66
- Prantzos, N., Abia, C., Limongi, M., Chieffi, A., & Cristallo, S. 2018, *MNRAS*, **476**, 3432
- Recio-Blanco, A., de Laverny, P., Worley, C., et al. 2012, *A&A*, **538**, A117
- Renda, A., Fenner, Y., Gibson, B. K., et al. 2004, *MNRAS*, **354**, 575
- Sieverding, A., Langanke, K., Martínez-Pinedo, G., et al. 2019, *ApJ*, **876**, 151
- Sieverding, A., Martínez-Pinedo, G., Huther, L., Langanke, K., & Heger, A. 2018, *ApJ*, **865**, 143
- Spitoni, E., Matteucci, F., Jönsson, H., Ryde, N., & Romano, D. 2018, *A&A*, **612**, A16
- Teltng, J. H., Avila, G., Buchhave, L., et al. 2014, *AN*, **335**, 41
- Timmes, F. X., Woosley, S. E., & Weaver, T. A. 1995, *ApJS*, **98**, 617
- Tody, D. 1993, in ASP Conf. Ser. 52: Astronomical Data Analysis Software and Systems II, ed. R. J. Hanisch, R. J. V. Brissenden, & J. Barnes (San Francisco, CA: ASP), 173
- Valenti, J. A., & Piskunov, N. 1996, *A&AS*, **118**, 595
- Valenti, J. A., & Piskunov, N. 2012, *SME: Spectroscopy Made Easy*, Astrophysics Source Code Library, ascl:1202.013
- Werner, K., Rauch, T., & Kruk, J. W. 2005, *A&A*, **433**, 641
- Woosley, S. E., Hartmann, D. H., Hoffman, R. D., & Haxton, W. C. 1990, *ApJ*, **356**, 272
- Woosley, S. E., & Haxton, W. C. 1988, *Natur*, **334**, 45
- Yuk, I.-S., Jaffe, D. T., Barnes, S., et al. 2010, *Proc. SPIE*, **7735**, 77351M